

Journal of Materials Chemistry C

Materials for optical, magnetic and electronic devices

Accepted Manuscript

This article can be cited before page numbers have been issued, to do this please use: Y. Otake, A. Isobe, T. Wang, C. Chueh, M. Wakioka and T. Michinobu, *J. Mater. Chem. C*, 2026, DOI: 10.1039/D6TC00601A.



This is an Accepted Manuscript, which has been through the Royal Society of Chemistry peer review process and has been accepted for publication.

Accepted Manuscripts are published online shortly after acceptance, before technical editing, formatting and proof reading. Using this free service, authors can make their results available to the community, in citable form, before we publish the edited article. We will replace this Accepted Manuscript with the edited and formatted Advance Article as soon as it is available.

You can find more information about Accepted Manuscripts in the [Information for Authors](#).

Please note that technical editing may introduce minor changes to the text and/or graphics, which may alter content. The journal's standard [Terms & Conditions](#) and the [Ethical guidelines](#) still apply. In no event shall the Royal Society of Chemistry be held responsible for any errors or omissions in this Accepted Manuscript or any consequences arising from the use of any information it contains.

1 **Cost-efficient quinoxaline-based semiconducting polymers: systematic structure–property–**
2 **morphology correlation toward reliable organic field-effect transistors**

3
4 Yuta Otake,^a Atsushi Isobe,^a Ting-Yu Wang,^b Chu-Chen Chueh,^b Masayuki Wakioka,^c and
5 Tsuyoshi Michinobu^{a,*}

6
7 ^a Department of Materials Science and Engineering, Institute of Science Tokyo, 2-12-1
8 Ookayama, Meguro-ku, Tokyo 152-8552, Japan

9 ^b Department of Chemical Engineering, National Taiwan University, Taipei 10617, Taiwan

10 ^c Sagami Chemical Research Institute, 2743-1 Hayakawa, Ayase, Kanagawa 252-1193, Japan
11 E-mail: michinobu@mct.isct.ac.jp

12 Electronic Supplementary Information (ESI) available. See DOI: 10.1039/x0xx00000x
13

14 **Abstract**

15 Achieving low-cost, organic semiconducting polymers remains a key challenge for the practical
16 application of organic field-effect transistors (OFETs). To overcome this issue, quinoxaline has
17 attracted considerable attention due to its unique structural advantages and synthetic feasibility. In
18 this study, a series of quinoxaline-based semiconducting polymers were successfully synthesized
19 through systematic tuning of π -linkers and alkyl side chains, with comprehensive evaluation of
20 their OFET performance. Density functional theory calculations revealed that these polymers
21 exhibit highly planar backbone structures stabilized by intramolecular noncovalent interactions.
22 Among the synthesized polymers, a thiophene-linker-incorporated polymer with a short alkyl
23 chain exhibited a hole mobility of $2.42 \times 10^{-2} \text{ cm}^2 \text{ V}^{-1} \text{ s}^{-1}$, representing an improvement of nearly
24 one order of magnitude over conventional PTQ10-based OFETs. Furthermore, the introduction of
25 a fluorinated bithiophene unit as the π -type linker enabled ambipolar charge transport. Grazing-
26 incidence wide-angle X-ray scattering (GIWAXS) results further revealed that all polymers
27 exhibited edge-on orientations conducive to efficient charge transport in OFETs. Collectively,



1 this study provides insights into structure–property–morphology relationships in quinoxaline-
2 based polymers with low synthetic complexity, providing rational molecular design guidelines for
3 scalable semiconducting polymer materials.

4

5 **1. Introduction**

6 Organic field-effect transistors (OFETs) and organic photovoltaic cells (OPVs) have attracted
7 considerable attention as core technologies for next-generation flexible electronics due to their
8 lightweight properties, mechanical flexibility, and compatibility with large-area printing
9 processes.^{1–4} Compared to small-molecule materials, semiconducting polymers exhibit superior
10 film-forming capabilities, thermal stability, and mechanical strength, enabling simplified device
11 fabrication through solution processing.⁵ Recent rapid breakthroughs in OFET and OPV
12 performance have been achieved through the development of precisely designed donor–acceptor
13 (D–A) copolymers.^{6–8} In OPVs, power conversion efficiencies (PCEs) have reached 20%.
14 Meanwhile, in OFETs, charge carrier mobilities in numerous systems have now surpassed 1 cm²
15 V^{–1} s^{–1}, rivaling those of inorganic materials.^{5,9–11}

16 Effective strategies for achieving high-performance semiconducting polymers involve
17 enhancing the planarity and rigidity of the conjugated backbone while extending the π -conjugation
18 to strengthen interchain interactions.^{12–14} As a result, many high-performance polymers reported
19 in recent years rely on complex fused-ring skeletons composed of multiple aromatic units.¹⁵
20 However, synthesizing such fused frameworks typically requires multistep organic reactions and
21 cumbersome purification processes, resulting in high synthesis costs. For example, the synthesis
22 of representative OPV donor materials, D18 and PM6, involves over 15 reaction steps, with
23 reported material costs exceeding \$200 g^{–1} (**Fig. 1a**).¹⁶ Similarly, high charge carrier mobilities in
24 OFETs were achieved through multi-step synthesis of complex fused aromatic cores, exemplified
25 by materials such as naphthalene diimide (NDI),^{17–19} indacenodithiophene (IDT),^{20,21}
26 diketopyrrolopyrrole (DPP),^{7,22,23} and bithiophene imide (BTI) (**Fig. 1b**).²⁴ In addition, the
27 extensive use of organic solvents and generation of substantial chemical waste during multistep
28 synthesis contribute to environmental pollution.^{25–27} These problems hinder the practical
29 implementation of semiconducting polymers.²⁸



1 To overcome this challenge, the field of organic electronics has recently made rapid
2 progress in polymer development—these polymers feature simple molecular structures that can be
3 easily synthesized through straightforward reaction steps yet exhibit high performance.^{29–32} A
4 representative material, poly[[6,7-difluoro[(2-hexyldecyl)oxy]-5,8-quinoxalinediyl]-2,5-
5 thiophenediyl]] (PTQ10), features a quinoxaline core (**Fig. 1a**).^{33–35} PTQ10 can be synthesized
6 from conventional starting chemicals in just five reaction steps.³⁶ Moreover, functionalization of
7 the quinoxaline moiety allows precise tuning of energy levels related to electron density and charge
8 transport properties.³⁷ Consequently, quinoxaline-based polymers have attracted considerable
9 interest as building blocks for low-cost, high-performance organic electronic materials.^{38–40} Recent
10 studies have also explored the application of quinoxaline-based donor polymers in OFETs.
11 PTQ10-based polymer reported by Campoy-Quiles and co-workers exhibited a hole mobility of
12 $2.45 \times 10^{-3} \text{ cm}^2 \text{ V}^{-1} \text{ s}^{-1}$.⁴¹ Guha and co-workers achieved comparable mobility by introducing
13 thienylenevinylene (TVT) units into the quinoxaline backbone (**Fig. 1c** and **Table S1**).⁴² However,
14 systematic investigations of PTQ10-based polymers in OFETs remain limited,^{43–47} as the
15 relationships between molecular structure, thin-film morphology, and device performance have
16 not been fully elucidated.

17 In this study, we synthesized a series of quinoxaline-based polymers by systematically
18 modifying their π -linker units and alkyl side-chain structures, and comprehensively investigated
19 their OFET performance. Density functional theory (DFT) calculations indicate that the
20 synthesized polymers adopt highly planar conformations through noncovalent interactions, such
21 as S–F and S–N interactions, conferring strong aggregation propensity, a property validated by
22 spectroscopic techniques. Thin-film transistors based on these polymers exhibited competitive
23 charge carrier mobilities relative to previously reported PTQ10-based polymers. Furthermore,
24 grazing-incidence wide-angle X-ray scattering (GIWAXS) measurements reveal the correlation
25 between molecular packing and charge transport properties (**Fig. 1d**).

26



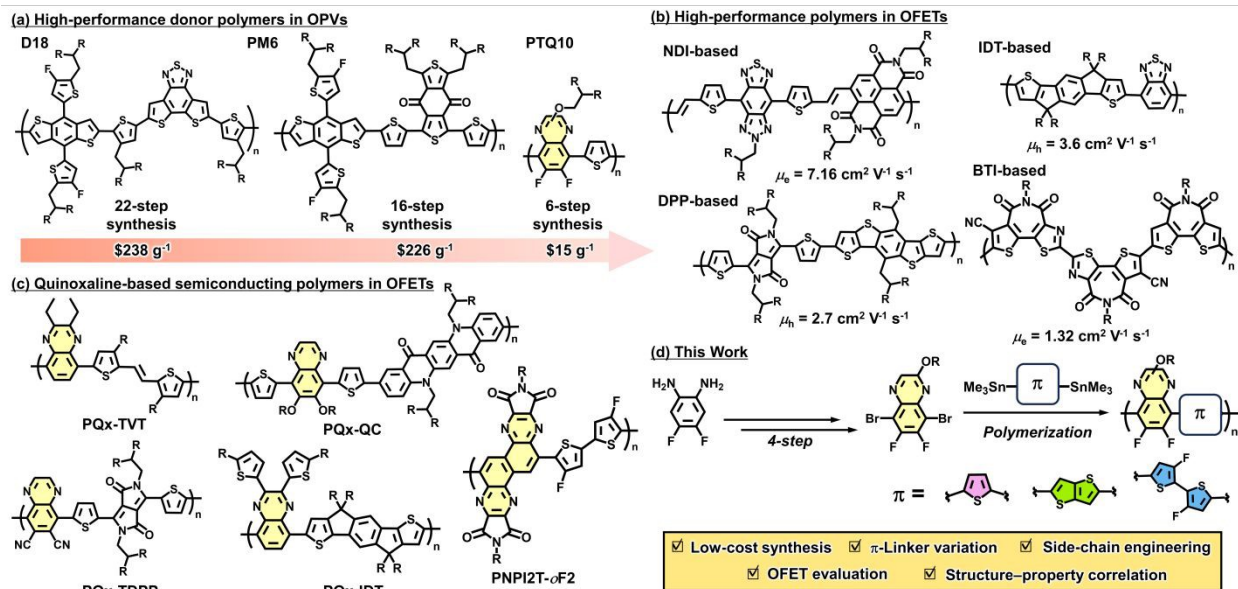


Fig. 1 Comparison of representative polymer semiconductors and the design concept of this work. (a) Representative high-performance donor polymers used in OPVs. (b) Representative high-performance polymer semiconductors for OFETs. (c) Previously reported quinoxaline-based semiconducting polymers for OFET applications. (d) This work: a cost-efficient quinoxaline-based polymer platform.

2. Results and discussion

2.1. Synthesis

The synthetic routes and polymerization conditions for quinoxaline-based monomers are summarized in **Scheme 1**. The dibromoquinoxaline derivative **Qx-3** was synthesized from commercially available 1,2-diamino-4,5-difluorobenzene (**1**) via previously reported procedure (**Scheme 1a**).³⁶ Notably, the intermediate was purified solely by precipitation without chromatographic purification, yielding a final overall yield of 71%. The monomer **Qx-4** was obtained by introducing a 2-hexyldecyl group onto **Qx-3** via a Mitsunobu reaction. Using the $P(\text{tert-Bu})_3\text{Pd G3}$ catalyst, **Qx-4** was polymerized with stannylated thiophene-based monomers via Stille coupling (**Scheme 1b**).⁴⁸ Detailed polymerization conditions employed in this study are summarized in **Table S2**. The polymerization of **P1**, containing a thiophene linker, proceeded homogeneously throughout. However, precipitation was observed during the polymerizations of

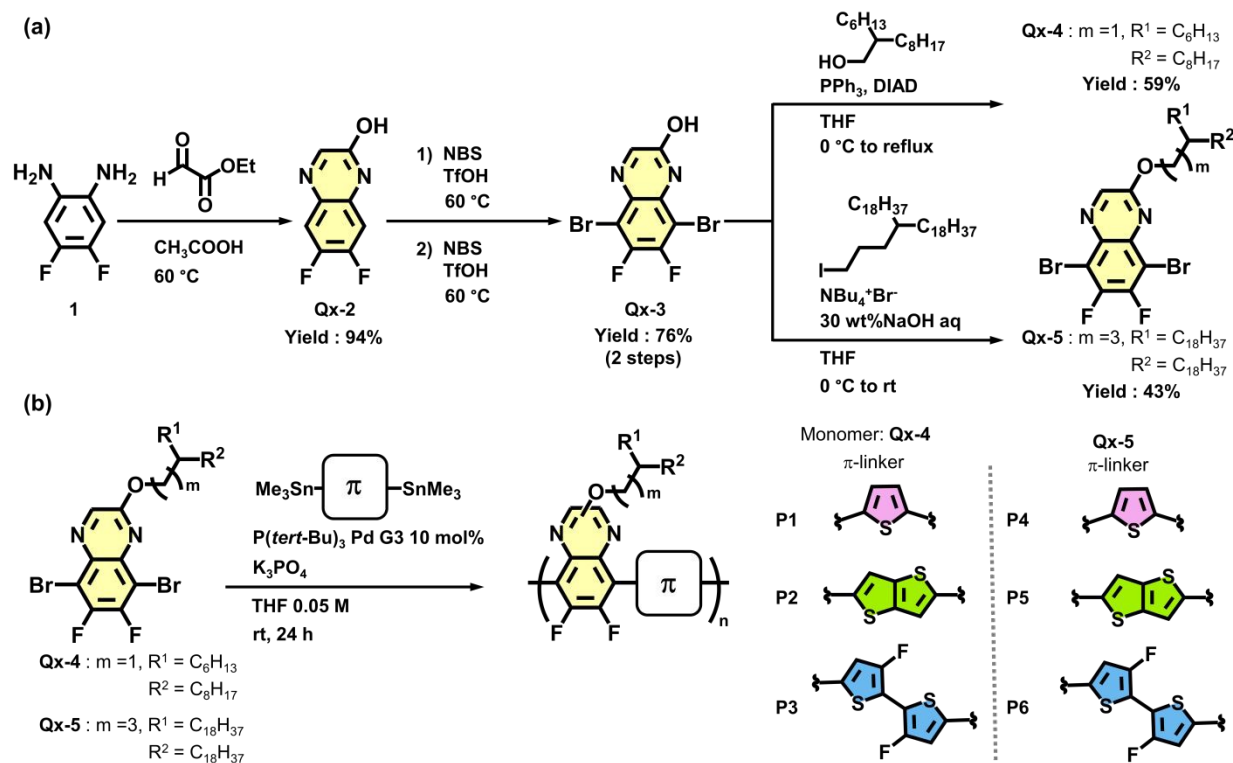


1 **P2** and **P3**, which contain thieno[3,2-*b*]thiophene or fluorinated bithiophene linkers. This behavior
2 is attributed to enhanced aggregation induced by the more planar donor units. After 24 h of
3 polymerization, all polymers were purified via Soxhlet extraction with methanol and acetone to
4 remove catalyst residues, residual monomers, and low-molecular-weight fractions. For **P1**, the
5 dichloromethane-extracted fraction was reprecipitated in methanol and collected by filtration. **P2**
6 and **P3** were obtained by reprecipitating the chloroform fraction collected after dichloromethane
7 extraction. Gel permeation chromatography (GPC) analysis revealed that the number-average
8 molecular weight (M_n) of **P1** was determined to be 10.8 kg mol⁻¹, while the M_n values of the poorly
9 soluble **P2** and **P3** were significantly reduced to 3.3 and 4.6 kg mol⁻¹, respectively (**Table 1** and
10 **Fig. S1a**). The reduced molecular weights of **P2** and **P3** likely stems from their strong aggregation
11 tendency, causing precipitation before growth into high-molecular-weight products. Consistent
12 with this finding, **P1** readily dissolves in common chlorinated solvents like chloroform and
13 chlorobenzene at room temperature, whereas **P2** and **P3** require heating to form homogeneous
14 solutions.

15 To obtain higher-molecular-weight polymers, polymer solubility must be enhanced to
16 suppress precipitation. Therefore, monomer **Qx-5** bearing a longer alkyl chain was synthesized via
17 the Williamson etherification reaction and polymerized under conditions similar to those for **Qx-**
18 **4** (**Scheme 1**). Even with thieno[3,2-*b*]thiophene or fluorinated bithiophene linkers, the extended
19 alkyl side chain suppressed precipitation, indicating significantly improved solubility of the
20 resulting polymers. After reactions, crude products were purified by Soxhlet extraction (same as
21 for **P1–P3**). **P4–P6** were obtained by reprecipitation of their hexane-extracted fractions in
22 methanol. GPC analysis revealed that the M_n values of **P4–P6** all exceeded 11 kg mol⁻¹,
23 substantially higher than those of the short-chain alkyl **Qx-4**-based polymers. These results suggest
24 that the enhanced solubility facilitated the attainment of high molecular weights (**Table 1** and **Fig.**
25 **S1b**). Furthermore, **P4–P6** dissolves in chloroform and chlorobenzene without heating, implying
26 high solution processability suitable for OFET fabrication.

27





Scheme 1 (a) Synthesis of quinoxaline-based monomers **Qx-4** (short alkyl side chains) and **Qx-5** (long alkyl side chains). (b) Synthesis of quinoxaline-based conjugated polymers **P1–P6** via Stille polycondensation using different π -linkers.

The synthetic complexity of quinoxaline-based polymers was evaluated using the Synthetic Complexity Index (SCI). SCI quantitatively assesses the synthetic complexity of polymers relative to reported materials by integrating factors such as the number of reaction steps, overall yields, number and type of purification processes, and hazardous chemical usage.^{49,50} Using an SCI value of 100 for the commonly used organic photovoltaic material donor D18 as a benchmark, the estimated SCI value for **P1** is 31.7.¹⁶ This value indicates that the synthetic complexity of **P1** has been reduced to one-third that of D18 (**Table 1** and **Table S3**). The reduced synthetic complexity of **P1** mainly originates from fewer reaction steps and simplified purification methods—in contrast to the D18 synthesis process, which requires 22 multistep reactions and column chromatography purification. In addition, the absence of hazardous reagents in the synthesis process significantly contributes to **P1**'s low SCI value. These results demonstrate that quinoxaline-based polymers are more suitable for large-scale production and can effectively reduce environmental impacts



1 compared to previously reported semiconducting polymers. Notably, diketopyrrolopyrrole (DPP)-
2 based polymers are widely used as key building blocks for high-performance OFETs,^{7,22,23} and
3 some derivatives, including fluorinated thiophene-DPP systems such as fDT-DPP, exhibit
4 ambipolar charge transport.⁵¹ However, these systems generally require more complex synthetic
5 procedures, whereas the present polymers exhibit SCI values in the range of 40–50, highlighting
6 their reduced synthetic complexity (**Table S4**).

7 To evaluate the thermal stability and phase transition behavior of **P1–P6**,
8 thermogravimetric analysis (TGA) and differential scanning calorimetry (DSC) measurements
9 were performed. The TGA curves showed that all polymers exhibited a 5% weight-loss
10 temperature (T_{5d}) above 300 °C, indicating sufficient thermal stability to meet the requirements
11 for OFET applications (**Table 1** and **Fig. S2**). In DSC measurements, **P1–P3** bearing short alkyl
12 chains showed no thermal transitions attributable to melting or crystallization during either heating
13 and cooling scans within the temperature range. In contrast, **P4–P6**, due to their longer alkyl chains,
14 exhibited endothermic peaks near 30 °C during heating and exothermic peaks during cooling,
15 which are attributed to the melting and crystallization of the long alkyl chains (**Fig. S3**).⁵²

16
17 **Table 1** Physicochemical properties and synthetic complexity of **P1–P6**.

	M_n^a / kg mol ⁻¹	M_w^a / kg mol ⁻¹	PDI ^{a, b}	Yield	SCI ^c	T_{5d}^d / °C
P1	10.8	20.1	1.86	27%	31.7	367.5
P2	3.3	5.4	1.62	45%	27.1	315.8
P3	4.6	9.5	2.07	21%	32.2	369.0
P4	23.5	43.6	1.85	85%	25.6	364.2
P5	11.2	25.7	2.29	76%	26.3	351.5
P6	13.1	26.9	2.06	66%	27.3	370.9

18 ^a Determined by GPC using 1,2-dichlorobenzene as the eluent at 40 °C.

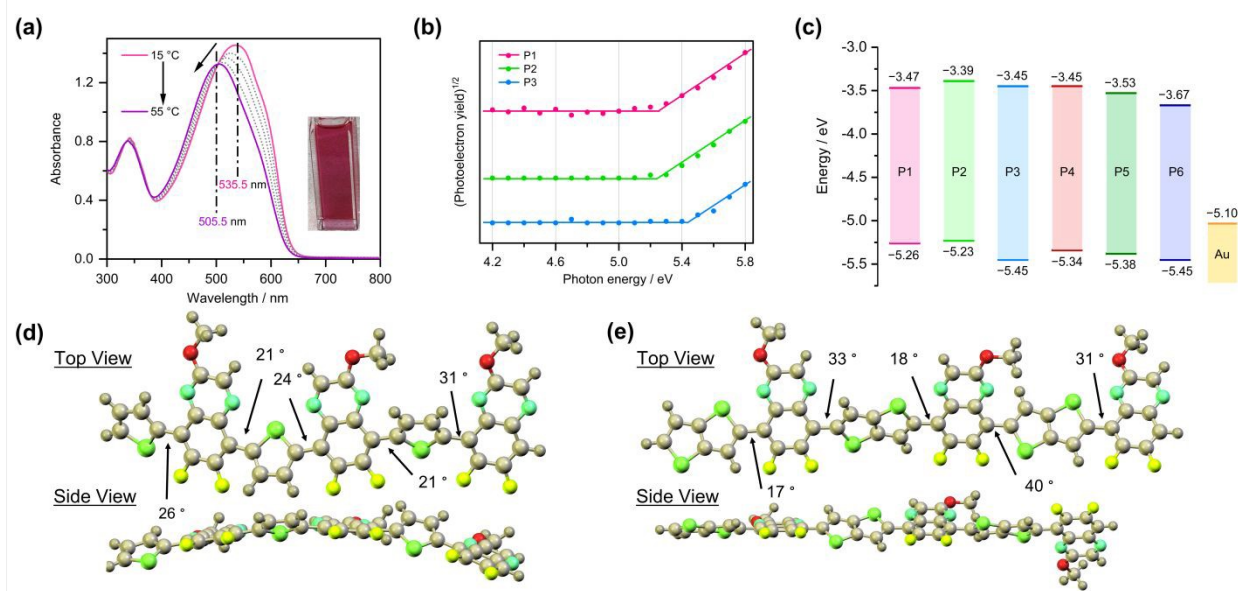
19 ^b Polydispersity index (M_w/M_n)

20 ^c Synthetic Complexity Index; A relative metric representing synthetic complexity, normalized to
21 the D18 synthesis as the reference (0–100).

22 ^d Temperature at 5% weight loss, determined by TGA.



1
2 **2.2. Optical and electrochemical properties and theoretical calculations**
3 To elucidate the influence of π -linkers on optical properties of the polymers, UV-vis absorption
4 spectroscopy measurements were performed. Under chloroform dilution conditions, all polymers
5 exhibited absorption bands in the 300–400 nm region (attributed to π - π^* transitions) and broad
6 absorption bands in the 400–700 nm region (attributed to intramolecular charge-transfer (ICT)
7 transitions).⁵³ Upon heating these solutions, the absorption maxima (λ_{max}) showed a pronounced
8 blue shift, accompanied by significant spectral shape changes (**Fig. 2a** and **Fig. S4–S7**). These
9 observations indicate partial dispersion of the polymer aggregates formed at room temperature
10 upon heating. Comparing the λ_{max} values of the dispersed polymers at 55 °C, those containing
11 thiophene linkers (**P1** and **P4**) exhibited more blue-shifted λ_{max} values (ca. 505 nm) compared to
12 the other polymers (**Table 2**). This result suggests that the photophysical properties are primarily
13 governed by the effective conjugated length, which is related to the electron-donating character of
14 the linker units and the backbone planarity. Upon cooling the heated solutions to 15 °C, the original
15 spectra were recovered, demonstrating the thermos-reversibility of the polymer aggregation (**Fig.**
16 **S4–S7**).⁵⁴
17



18



1 **Fig. 2** (a) Temperature-dependent UV–vis absorption spectra of **P1** dissolved in chloroform
2 solution ($c = \text{ca. } 1.0 \times 10^{-5} \text{ M}$) recorded from 15 to 55 °C. (b) PYS spectra of **P1–P3** in the thin-
3 film state. (c) Energy level diagram of **P1–P6** in the thin-film state estimated from PYS
4 measurements. The work function of Au is included for comparison. (d, e) Optimized geometries
5 and conformational analysis of (d) **P1**, **P4** and (e) **P2**, **P5** models calculated at the $\omega\text{B97XD}/6$ -
6 $31\text{G}(\text{d}, \text{p})$ level.

7
8 To theoretically elucidate the differential effects of π -linkers on absorption and aggregation
9 properties, trimer models were subjected to structural optimization and natural bond orbital (NBO)
10 analysis using density functional theory (DFT, $\omega\text{B97XD}/6$ - $31\text{G}(\text{d}, \text{p})$ level). The optimized
11 backbone structures are shown in **Fig. 2d**, **2e**, and **S8**, with the corresponding molecular orbitals
12 depicted in **Fig. S9**. Across all thiophene-based donor models, the dihedral angles between
13 adjacent units ranged from 0 to 40°. Structural comparisons revealed that the thiophene-
14 incorporated models exhibited twisted conformations, whereas the introduction of thieno[3,2-
15 *b*]thiophene and fluorinated bithiophene resulted in more planar backbone structures. Both models
16 confirm intramolecular S–N and S–F interactions with spatial penetration. The interatomic
17 distances in the optimized structures were approximately 0.27–0.28 nm for S–N and 0.28–0.29 nm
18 for S–F. These distances were shorter than the sum of the corresponding van der Waals radii,
19 suggesting weak noncovalent interactions.³² Unlike thiophene, the extended thieno[3,2-
20 *b*]thiophene and fluorinated bithiophene units showed stronger S–N and S–F interactions. These
21 interactions suppress conformational freedom around the bond axis, leading to a more planar and
22 rigid backbone. Notably, the fluorinated bithiophene model showed the highest planarity due to
23 the multipoint nature of these interactions. The NBO analysis further confirmed the orbital
24 interactions corresponding to S–N and S–F bonds, corroborating the planarity of the backbone
25 (**Fig. S9**).^{32,55}

26 The energy levels of **P1–P6** were evaluated via photoelectron yield spectroscopy (PYS)
27 and cyclic voltammetry (CV) (**Table 2**, **Fig. 2b**, **2c**, and **S10**). PYS measurements were conducted
28 in air, with film preparation following the same procedures as for OFET devices exhibiting the
29 highest carrier mobilities (vide infra). Although all polymers exhibited similar HOMO energy
30 levels within the range of –5.23 to –5.45 eV, **P3** and **P6** featured deeper HOMO levels than the
31 other polymers due to the electron-withdrawing nature of fluorine atom in their donor units. CV



1 measurements revealed well-defined redox waves for all polymers. Their HOMO energy levels,
2 referenced to the ferrocene/ferrocenium redox couple, show good agreement with PYS estimates
3 (see **Tables 2** and **S5** and **Fig. S11**). The LUMO energy levels estimated by combining optical
4 band gaps and PYS-determined HOMO levels ranged from -3.39 to -3.67 eV, consistent with
5 electrochemical measurements. These energy levels suggest that gold (Au) with a work function
6 of -5.1 eV is suitable for both hole and electron injection in OFET devices based on **P1–P6**.^{56,57}

8 **Table 2** Optical absorption and energy levels of polymers **P1–P6**.

	$\lambda_{\max}^{\text{sol } a}$	$\lambda_{\max}^{\text{film}}$	$E_{\text{opt}^{\text{gap}} }^b$	E_{HOMO}^c	E_{LUMO}^d
	/ nm	/ nm	/ eV	/ eV	/ eV
P1	505.5	554, 597.5	1.79	-5.26	-3.47
P2	531	562, 609.5	1.84	-5.23	-3.39
P3	523.5	560, 616.5	1.83	-5.45	-3.45
P4	504	557.5, 607.5	1.89	-5.34	-3.45
P5	569	572, 622	1.85	-5.38	-3.53
P6	554.5	557.5, 607.5	1.78	-5.45	-3.67

9 ^a The maximum absorption wavelengths were determined from solution UV–vis spectra measured
10 at 55 °C.

11 ^b The optical band gaps ($E_{\text{opt}^{\text{gap}}}$) were estimated from the absorption onset of the thin film UV–vis
12 spectra.

13 ^c The HOMO energy levels (E_{HOMO}) were determined by PYS using thin films fabricated under
14 the same conditions as the OFET devices.

15 ^d Estimated as $E_{\text{LUMO}} = E_{\text{HOMO}} + E_{\text{opt}^{\text{gap}}}$

17 2.3. Charge transport properties in OFET devices

18 The charge-transport properties of quinoxaline-based polymers were investigated by fabricating
19 top-contact/bottom-gate (TC/BG) polymer thin-film transistors (**Fig. S12**). The organic
20 semiconductor layers were formed by spin-casting polymer solutions ($c = \text{ca. } 4\text{--}6$ g L⁻¹ in
21 chloroform) onto SiO₂ (300 nm)/N⁺⁺-Si substrates modified with octadecyltrimethoxysilane
22 (OTMS) self-assembled monolayers (SAMs) in a nitrogen-filled glovebox. After thermal

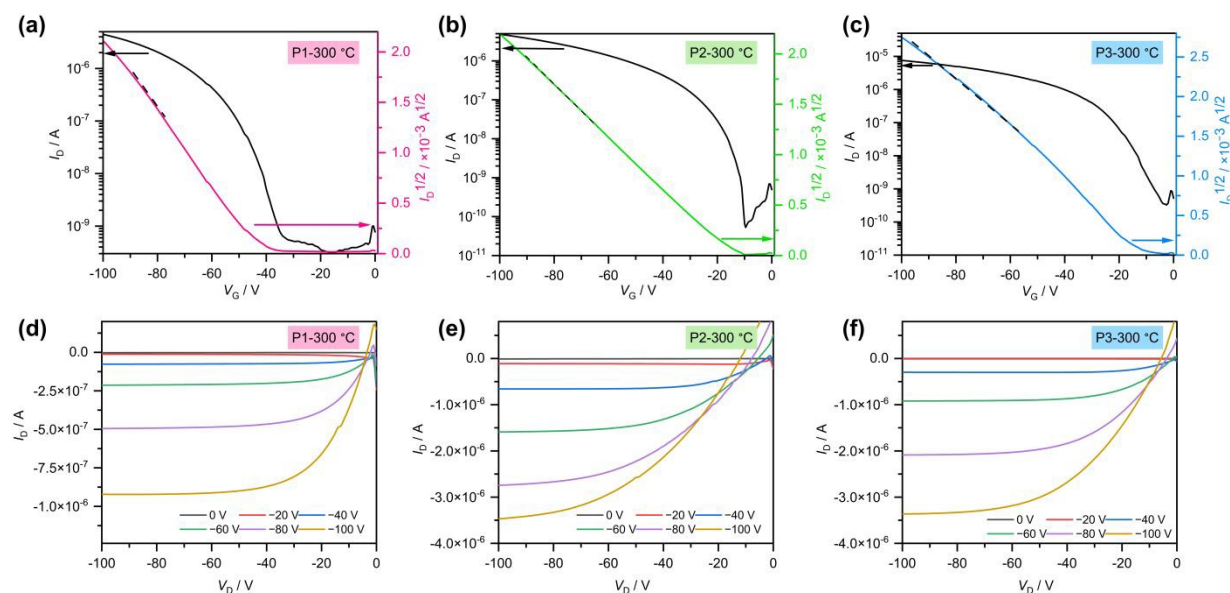


1 annealing at temperatures ranging from 100 to 300 °C, gold source and drain electrodes were
2 deposited via thermal evaporation. Detailed device fabrication procedures are provided in the
3 Supporting Information.⁵⁶ p-Type OFET characteristics were evaluated in air for all devices. For
4 **P6**, both p- and n-type characteristics were also evaluated under vacuum conditions to ensure a
5 reliable assessment of ambipolar transport. Current–voltage curves for devices fabricated based on
6 **P1–P6** are shown in **Fig. 3** and **S13–S15**, with extracted parameters summarized in **Table 3**.

7 **P1–P5** exhibited unipolar p-type charge transport behavior, whereas **P6** demonstrated a
8 balanced ambipolar behavior with a hole-to-electron mobility ratio (μ_h/μ_e) of 0.99, as measured
9 under vacuum conditions for both p- and n-type operation. This behavior is likely associated with
10 the fluorinated linker unit and superior film morphology of **P6** result in a lower electron injection
11 barrier (Schottky barrier) between it and gold electrodes compared to other polymers, collectively
12 enabling ambipolar charge transport.⁵⁸ It is generally expected that electron injection from gold
13 electrodes is less favorable than hole injection due to the larger energetic offset between the
14 electrode work function and the LUMO level compared to the HOMO level. However, transfer
15 line method (TLM) analysis revealed that the contact resistance for hole transport was higher than
16 that for electron transport ($R_{C,e} W = 3.24 \times 10^7 \Omega \cdot \text{cm}$ at $V_G = -100 \text{ V}$ and $R_{C,e} W = 5.18 \times 10^6 \Omega \cdot \text{cm}$
17 at $V_G = +100 \text{ V}$, respectively; **Fig. S16** and **Table S6**).⁵⁹ These results indicate that, although hole
18 injection is energetically more favorable, electron transport may benefit from lower contact
19 resistance, which could result in comparable charge carrier mobilities. Among all polymers, **P1**
20 annealed at 300 °C exhibited the highest average hole mobility of $2.45 \times 10^{-2} \text{ cm}^2 \text{ V}^{-1} \text{ s}^{-1}$ (**Fig.**
21 **3a**). Compared to previously reported PTQ10-based polymers employing a quinoxaline scaffold,
22 the hole mobility of **P1** is approximately one order of magnitude higher (**Table S1**). **P2** and **P3**
23 exhibited hole mobilities approximately half that of **P1** (**Fig. 3b** and **3c**). While increasing the
24 annealing temperature enhanced the hole mobility for **P1–P3**, excessive annealing caused a
25 decrease in mobility for **P4–P6**, which possess longer alkyl side chains. Notably, the charge
26 transport property of **P4** was completely impaired after 100 °C annealing (**Fig. S17**). This behavior
27 arises from thermal activation of the long alkyl chains at elevated temperatures, which disrupts the
28 molecular ordering within the film. Consequently, despite being the highest molecular weight
29 polymer synthesized, **P4** exhibited a mobility two orders of magnitude lower than **P1**. Variations
30 in molecular weight among **P1–P6** may influence the observed device performance, but the
31 backbone structure appears to be the primary determining factor.^{18,60} For instance, the hole



1 mobility of **P4** was much lower than those of **P5** and **P6**, which employed thieno[3,2-*b*]thiophene
2 and fluorinated bithiophene linkers, respectively. This result suggests that enhanced backbone
3 planarity in **P5** and **P6** is likely to promote aggregation, which may contribute to improved
4 molecular ordering in the thin films, consistent with the absorption spectroscopy and DFT results..
5



6
7 **Fig. 3** Transfer characteristics (I_D – V_G) of OFET devices fabricated from (a) **P1**, (b) **P2**, and (c) **P3**
8 thin films after thermal annealing at 300 °C, measured in air at a fixed drain voltage of $V_D = -100$
9 V. Output characteristics (I_D – V_D) of the corresponding devices are shown for (d) **P1**, (e) **P2**, and
10 (f) **P3**, measured at gate voltages ranging from 0 to –100 V.

11
12 **Table 3** Summary of OFET performance parameters, including charge carrier mobility (μ),
13 threshold voltage (V_{th}), and current on/off ratio (I_{on}/I_{off}), for polymers **P1**–**P6** under optimized
14 annealing conditions.

Polymer	Annealing	Operation mode	Condition	μ (μ_{max}) ^a / $\text{cm}^2 \text{V}^{-1} \text{s}^{-1}$	V_{th} / V	I_{on}/I_{off} ^b
P1	300 °C	p-type	In air	$(2.45 \pm 0.31) \times 10^{-2}$	–36.9	10^3 – 10^4
				(2.78×10^{-2})	± 4.1	
P2	300 °C	p-type	In air	$(1.04 \pm 0.09) \times 10^{-2}$	–11.3	10^2 – 10^5



				(1.18×10^{-2})	± 3.6	
P3	300 °C	p-type	In air	$(1.46 \pm 0.12) \times 10^{-2}$	-6.8	10^4 – 10^6
				(1.58×10^{-2})	± 7.2	
P4	as cast	p-type	In air	$(1.50 \pm 1.37) \times 10^{-4}$	-36.9	10^2 – 10^4
				(3.20×10^{-4})	± 14.7	
P5	200 °C	p-type	In air	$(2.25 \pm 0.51) \times 10^{-3}$	-22.5	10^0 – 10^1
				(2.62×10^{-3})	± 8.3	
	200 °C	p-type	In air	$(9.26 \pm 4.42) \times 10^{-4}$	-26.0	10^1
				(1.59×10^{-3})	± 14.7	
P6	200 °C	p-type	Under vacuum	$(1.07 \pm 0.23) \times 10^{-3}$	-11.0	10^1 – 10^2
				(1.45×10^{-3})	± 6.2	
	200 °C	n-type	Under vacuum	$(1.08 \pm 0.45) \times 10^{-3}$	-23.2	10^1 – 10^2
				(1.60×10^{-3})	± 21.7	

^a The values are presented as mean \pm standard deviation (SD) obtained from five independent OFET devices, and the values in parentheses correspond to the highest mobility.

^b $I_{\text{on}}/I_{\text{off}}$ ratios are reported as order-of-magnitude ranges estimated from the transfer characteristics.

2.4 Film morphology

To elucidate the relationship between the chemical structures of **P1**–**P6** and their carrier mobilities, we systematically investigated the thin-film morphology and polymer orientation using UV–vis absorption spectroscopy, GIWAXS, and atomic force microscopy (AFM). UV–vis absorption spectra of the polymer films revealed bathochromic shifts in the absorption maxima for all polymers compared to their partially dispersed state in chloroform (**Fig. S18**). In addition, the thin-film spectra revealed a significant increase in the absorption intensities of the 0–0 vibronic peaks. This spectral trend resembles phenomena observed during the cooling of dilute solutions. After annealing treatment, the absorption intensities of the 0–0 vibronic peaks slightly increased, indicating a rearrangement of polymer chains.

The surface morphology of the films was examined using AFM. For films of **P1** and **P4** incorporating thiophene π -linkers, the AFM images exhibited relatively uniform granular morphology (**Fig. S19** and **S20**). After annealing at 300 °C, structural enlargement was observed,



1 while the root-mean-square (RMS) roughness of **P1** increased from 2.81 to 10.7 nm (**Fig. 4a** and
2 **S19**). Notably, the annealed **P4** showed surface morphology disruption, inhibiting chain
3 rearrangement, which is consistent with restricted chain mobility at elevated temperatures (**Fig.**
4 **S20**). To further understand the thermal instability of **P4**, AFM measurements were performed
5 after thermal annealing at 100 °C and 200 °C (**Fig. S21**). With increasing annealing temperature,
6 the long alkyl side chains became more mobile, leading to local aggregation and morphological
7 disorder. Such structural changes are likely to disrupt charge percolation pathways, which explains
8 the complete loss of OFET performance after annealing. Other polymers possessing highly planar
9 backbone conformations formed nanofibrillar structures immediately after spin-coating.⁶¹ The
10 morphological differences between **P1** and **P4** suggest that introducing thieno[3,2-*b*]thiophene or
11 fluorinated bithiophene units enhances interchain interactions. Thermal annealing promotes
12 structural transformation from short, fine fibrous structures to larger aggregates through polymer
13 chain rearrangement (**Fig. 4b, 4c, S19, and S20**).

14 To investigate the polymer stacking structure in the thin films, films were prepared on Si
15 substrates using the same procedures as device fabrication and subjected to GIWAXS
16 measurements. The resulting two-dimensional diffraction images and one-dimensional patterns in
17 the out-of-plane and in-plane directions are shown in **Fig. 4d–g** and **S22**. Structural parameters
18 extracted from the out-of-plane lamellar diffraction peaks, including q_z , interlayer distance
19 (d_{lamellar}), full width at half maximum (FWHM), and crystal coherence length (CCL), are
20 summarized in **Tables 4** and **S7**. After annealing, all polymers exhibited diffraction peaks
21 attributable to lamellar (h00) orientation exclusively in the out-of-plane direction. This diffraction
22 pattern exhibits the characteristic of edge-on orientation, which may be beneficial for charge
23 transport in OFETs.⁶² Notably, when **P1** is used as a p-type material in OPV devices, it has been
24 reported in the literature to adopt a face-on orientation.^{54,63} This likely stems from the differing
25 deposition conditions between OPV and OFET. In OPV fabrication, **P1** was co-deposited with
26 acceptor materials onto a hydrophilic PEDOT:PSS layer, rather than onto hydrophobic SAM-
27 modified Si substrates employed in the present OFET devices. The full width at half maximum
28 (FWHM) of the diffraction peaks for **P2** was larger than that for **P1**, indicating lower crystallinity.
29 This reduced crystallinity may be related to lower hole mobility of **P2** compared to **P1**. Although
30 **P1–P3** displayed (100) and (200) crystal planes originating from lamellar ordering, **P4** with long
31 alkyl side chains exhibited diffraction peaks extending to the (300) crystal plane (**Fig. 4** and **S22**).



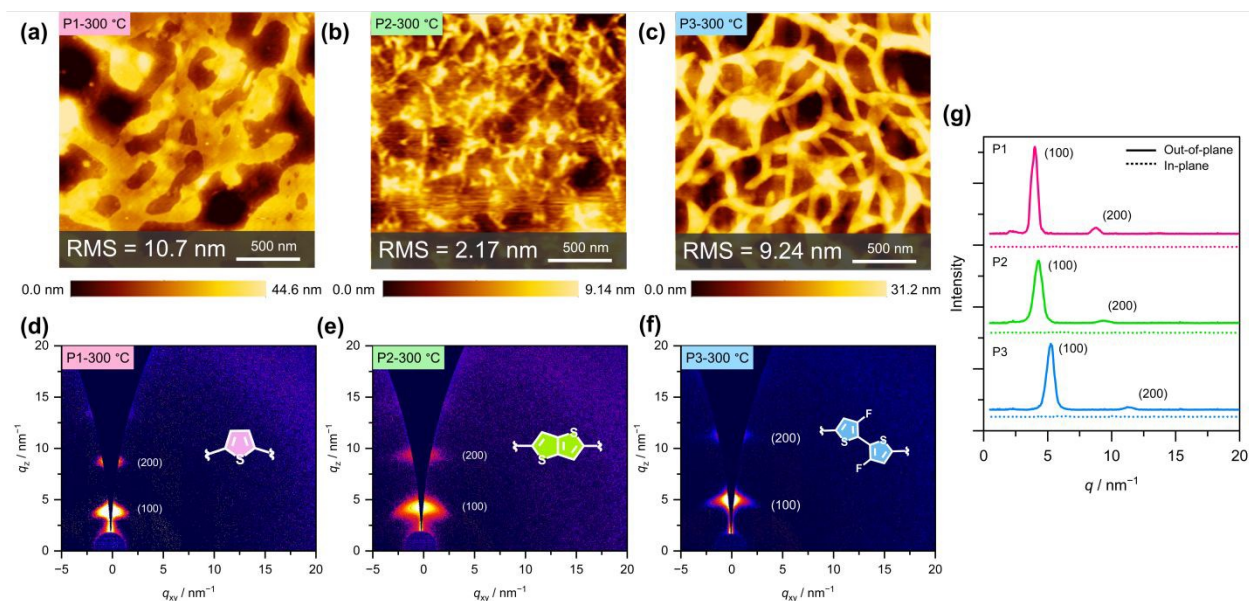
1 By employing thieno[3,2-*b*]thiophene and fluorinated bithiophene linkers, **P5** and **P6** exhibited
2 diffraction peaks attributable to (400) and (500) crystal planes, respectively (**Fig. S22**). These
3 results suggest that the elongation of the alkyl side chains enhances van der Waals interactions
4 through interdigitated arrangements between alkyl chains, leading to the formation of lamellar
5 structures with longer-range order. The higher-order lamellar diffraction peaks of **P5** and **P6** were
6 more distinct than those of **P4**, indicating improved lamellar ordering in the films. This enhanced
7 ordering may contribute, together with other factors such as backbone planarity and molecular
8 ordering, to the higher hole mobilities observed for **P5** and **P6** compared to **P4**. Although the
9 charge carrier mobility of **P4–P6** is relatively low in the present study, their relatively high
10 crystallinity suggests that the molecular design is fundamentally appropriate for efficient charge
11 transport. The limited performance is therefore more likely attributed to insufficient film
12 morphology optimization rather than intrinsic material limitations. Further optimization of
13 processing conditions is expected to unlock their full potential.

14 Notably, although UV–vis absorption measurements indicate aggregation in quinoxaline-
15 based polymer films, no distinct diffraction peaks originating from the (010) crystal plane
16 (corresponding to π – π stacking) were observed for any polymer. This may result from the random
17 regioregularity due to the asymmetric structure of the quinoxaline monomer. As the alkyl side
18 chains are randomly oriented, the polymer backbone may undergo distortion due to steric
19 hindrance. The asymmetric structure and reduced planarity may collectively impede the formation
20 of uniform π – π stacking.⁶⁴

21 Finally, device stability was evaluated via storage in a nitrogen-filled glovebox (**Fig. S23**).
22 These measurements correspond to the storage stability of the devices under an inert atmosphere.
23 Time-dependent measurements of hole mobility revealed that the performance of **P1** decreased to
24 48% of its initial value after 21 days; **P2** and **P3** decreased to ca. 20% and 5%, respectively, within
25 15 days. In contrast, **P4–P6** with longer alkyl side chains maintained hole mobility exceeding 70%
26 of their initial values after 17 days. This enhanced stability is likely associated with increased
27 molecular weight, improved crystallinity, and greater hydrophobicity—properties that effectively
28 mitigate device deterioration caused by moisture and oxygen permeation.^{65,66} Furthermore, to
29 evaluate operational stability, transfer characteristics of **P1**, which exhibited the highest mobility
30 in this study, were measured over 50 consecutive cycles in air (**Fig. S24**). No noticeable differences



1 were observed between the 1–25 and 26–50 cycles, suggesting stable device operation under the
2 tested conditions.¹⁹



4
5 **Fig. 4** AFM height images of polymer thin films annealed at 300 °C: (a) **P1**, (b) **P2**, and (c) **P3**.
6 The RMS roughness values are indicated in each panel (scan size: $2 \times 2 \mu\text{m}^2$). GIWAXS patterns
7 of the corresponding thin films after annealing at 300 °C: (d) **P1**, (e) **P2**, and (f) **P3**. (g) One-
8 dimensional line cuts extracted from the GIWAXS patterns along the out-of-plane (solid lines) and
9 in-plane (dotted lines) directions, highlighting the (100) lamellar stacking and the higher-order
10 (200) diffraction peaks.

11
12 **Table 4** Out-of-plane (100) lamellar packing parameters of polymers **P1–P6** evaluated by
13 GIWAXS.

	Annealing	Out-of-plane (100)			
		q_z / nm^{-1}	$d_{\text{lamellar}} / \text{nm}$	FWHM/ nm^{-1}	CCL/ nm
P1	300 °C	3.98	1.58	0.679	8.33
P2	300 °C	4.27	1.47	0.743	7.61
P3	300 °C	5.23	1.20	0.679	8.33
P4	as cast	2.09	3.01	0.297	19.0
P5	200 °C	2.09	3.00	0.287	19.7



P6	200 °C	2.28	2.75	0.534	10.6
-----------	--------	------	------	-------	------

1

2 **3. Conclusion**

3 In this study, we successfully synthesized a series of semiconducting polymers based on a
4 quinoxaline core through a simple and low-cost synthesis procedure. By systematically varying
5 the π -linker units and alkyl side-chain lengths, quinoxaline-based polymers **P1–P6** were
6 synthesized, and their OFET performances and thin-film structures were comprehensively
7 evaluated. Within this series, **P1** exhibited the highest average hole mobility of $2.45 \times 10^{-2} \text{ cm}^2$
8 $\text{V}^{-1} \text{ s}^{-1}$, representing an improvement over PTQ10-based OFETs. Extending the π -linker enhances
9 backbone planarity and promotes aggregation through intramolecular noncovalent interactions, yet
10 yields lower hole mobilities than **P1**. Conversely, combining a fluorinated bithiophene π -linker
11 with a longer alkyl chain achieved balanced ambipolar charge transport properties. GIWAXS
12 revealed that despite variations in π -linker units and alkyl chain lengths, all polymers formed edge-
13 on orientations, conducive to efficient charge transport in OFETs. In polymers bearing long alkyl
14 side chains, replacing the thiophene linker with thieno[3,2-*b*]thiophene or fluorinated bithiophene
15 enhanced backbone planarity and strengthened intermolecular interactions. These results
16 demonstrate that π -linker engineering effectively modulates backbone planarity, intermolecular
17 interactions, and thin-film crystallinity, which may influence charge transport properties.
18 Furthermore, the synergistic effects of the fluorinated comonomer and long alkyl side chains
19 enabled polymer thin films to form structures conducive to electron transport, thereby achieving
20 ambipolar charge transport in **P6**. Combining π -linker optimization with control over molecular
21 orientation through side-chain regioregularity holds promise for further enhancing charge transport
22 properties.^{67–69} Overall, this study provides insights into rational molecular design principles for
23 developing quinoxaline-based semiconducting polymers with low synthetic complexity and
24 scalable material frameworks, providing practical guidelines for next-generation organic field-
25 effect transistors.

26

27 **Author contributions**



1 Y.O. performed all experimental work, including the synthesis of all polymers, device fabrication
2 and performance evaluation, calculations, and data analysis (including GIWAXS), as well as
3 validation, visualization, writing – original draft, and writing – review & editing. A.I. contributed
4 to methodology development, data analysis, validation, supervision, funding acquisition, writing
5 – original draft, and writing – review & editing. T.-Y.W. performed the GIWAXS measurements.
6 C.-C.C. supervised the GIWAXS measurements and contributed to validation, writing – review &
7 editing. M.W. provided technical advice, contributed to validation, and engaged in fruitful
8 discussions regarding the polymerization. T.M. contributed to conceptualization, funding
9 acquisition, methodology, project administration, supervision, and writing – review & editing. All
10 authors have given approval to the final version of the manuscript.

11 **Conflicts of interest**

13 The authors have no conflicts of interest.

15 **Acknowledgements**

16 This study was partly supported by JSPS KAKENHI Grant Number JP24H0005 (T.M.) and
17 JP24K23077 (A.I.). Computational calculations were carried out using the TSUBAME4.0
18 supercomputer at the Institute of Science Tokyo, particularly for DFT calculations. The authors
19 also acknowledge the National Synchrotron Radiation Research Center (NSRRC) of Taiwan for
20 the GIWAXS experiments in BL23A1 (TLS).

22 **References**

- 23 1 X. Wu, W. Fu and H. Chen, *ACS Appl. Polym. Mater.*, 2022, **4**, 4609–4623.
- 24 2 X. Xu, Y. Zhao and Y. Liu, *Small*, 2023, **19**, 202206309.
- 25 3 X. Wan, C. Li, M. Zhang and Y. Chen, *Chem. Soc. Rev.*, 2020, **49**, 2828–2842.
- 26 4 J. Yi, G. Zhang, H. Yu and H. Yan, *Nat. Rev. Mater.*, 2024, **9**, 46–62.
- 27 5 H. Chen, W. Zhang, M. Li, G. He and X. Guo, *Chem. Rev.*, 2020, **120**, 2879–2949.
- 28 6 Y. Wang and T. Michinobu, *J. Mater. Chem. C*, 2016, **4**, 6200–6214.



- 1 7 Y. Wang and T. Michinobu, *J. Mater. Chem. C*, 2018, **6**, 10390–10410.
- 2 8 X. Liu, C. L. Anderson and Y. Liu, *Acc. Chem. Res.*, 2023, **56**, 1669–1682.
- 3 9 C. Wang, X. Zhang, H. Dong, X. Chen and W. Hu, *Adv. Energy Mater.*, 2020, **10**, 2000955.
- 4 10 S. Shoaee, H. M. Luong, J. Song, Y. Zou, T. Q. Nguyen and D. Neher, *Adv. Mater.*, 2024,
5 **36**, 2302005.
- 6 11 L. Luo, W. Huang, C. Yang, J. Zhang and Q. Zhang, *Front. Phys.*, 2021, **16**, 33500.
- 7 12 J. Lee, *Asian J. Org. Chem.*, 2023, **12**, e202300104.
- 8 13 K. C. Chong, T. L. D. Tam, R. Tao, K. L. O. Chin, M. H. Chua and J. Xu, *Energy Mater.*
9 *Adv.*, 2025, **6**, 0134.
- 10 14 A. Insuasty, S. Maniam and S. J. Langford, *Chem. Eur. J.*, 2019, **25**, 7058–7073.
- 11 15 H. Jiang, S. Zhu, Z. Cui, Z. Li, Y. Liang, J. Zhu, P. Hu, H. L. Zhang and W. Hu, *Chem.*
12 *Soc. Rev.*, 2022, **51**, 3071–3122.
- 13 16 J. J. Rech, J. Neu, Y. Qin, S. Samson, J. Shanahan, R. F. Josey, H. Ade and W. You,
14 *ChemSusChem*, 2021, **14**, 3561–3568.
- 15 17 M. Liao, J. Duan, P. Peng, J. Zhang and M. Zhou, *RSC Adv.*, 2020, **10**, 41764–41779.
- 16 18 Y. Wang, T. Hasegawa, H. Matsumoto, T. Mori and T. Michinobu, *Adv. Mater.*, 2018, **30**,
17 1707164.
- 18 19 Y. Wang, T. Hasegawa, H. Matsumoto and T. Michinobu, *J. Am. Chem. Soc.*, 2019, **141**,
19 3566–3575.
- 20 20 A. Wadsworth, H. Chen, K. J. Thorley, C. Cendra, M. Nikolka, H. Bristow, M. Moser, A.
21 Salleo, T. D. Anthopoulos, H. Sirringhaus and I. McCulloch, *J. Am. Chem. Soc.*, 2020, **142**, 652–
22 664.
- 23 21 X. Zhang, H. Bronstein, A. J. Kronemeijer, J. Smith, Y. Kim, R. J. Kline, L. J. Richter, T.
24 D. Anthopoulos, H. Sirringhaus, K. Song, M. Heeney, W. Zhang, I. McCulloch and D. M.
25 DeLongchamp, *Nat. Commun.*, 2013, **4**, 2238.
- 26 22 H. J. Cheon, T. K. An and Y. H. Kim, *Macromol. Res.*, 2022, **30**, 71–84.
- 27 23 S. Park, B. T. Lim, B. Kim, H. J. Son and D. S. Chung, *Sci. Rep.*, 2014, **4**, 5482.
- 28 24 Y. Li, S. Gámez-Valenzuela, W. Yang, R. Ding, Y. Wei, E. Huang, X. Guo and K. Feng,
29 *Macromolecules*, 2025, **58**, 7593–7604.
- 30 25 M. Ferrara, F. Della Negra and M. Verzini, *Org. Process Res. Dev.*, 2025, **29**, 1110–1124.
- 31 26 W. Liu, H. Shang, X. Xu and Z. Bo, *ACS Appl. Eng. Mater.*, 2025, **3**, 1102–1129.
- 32 27 M. Wakioka, *Polym. J.*, 2026, **58**, 103–116.



- 1 28 Y. H. Shih, G. L. Wu, P. H. Chueh, J. C. Chen, C. Y. Tsai, T. Y. Wang, M. H. Yu, Y. P.
2 Li, W. C. Chen and C. C. Chueh, *JACS Au*, 2025, **5**, 1382–1391.
- 3 29 N. Yang, Y. Cui, Y. Xiao, Z. Chen, T. Zhang, Y. Yu, J. Ren, W. Wang, L. Ma and J. Hou,
4 *Angew. Chem. Int. Ed.*, 2024, **63**, e202403753.
- 5 30 K. Yamanaka, T. Mikie and I. Osaka, *Adv. Energy Mater.*, 2025, **15**, 2502173.
- 6 31 K. Yamada, W. Suzuki, M. Kubota, J. Inamoto, M. Kondo, T. Koganezawa, Y. Chiga, R.
7 Takahata, T. Teranishi, H. Imahori and T. Umeyama, *J. Mater. Chem. C*, 2025, **13**, 7984–7995.
- 8 32 Z. Li, R. Ding, X. Gu, C. Zhang, J. Lv, Y. Han, J. Chen, Y. Cai, X. Zhang and H. Huang,
9 *Chem. Commun.*, 2025, **61**, 8659–8662.
- 10 33 C. Sun, F. Pan, H. Bin, J. Zhang, L. Xue, B. Qiu, Z. Wei, Z. G. Zhang and Y. Li, *Nat.*
11 *Commun.*, 2018, **9**, 743.
- 12 34 C. Sun, S. Qin, R. Wang, S. Chen, F. Pan, B. Qiu, Z. Shang, L. Meng, C. Zhang, M. Xiao,
13 C. Yang and Y. Li, *J. Am. Chem. Soc.*, 2020, **142**, 1465–1474.
- 14 35 A. L. Jones, C. H. Y. Ho, S. A. Schneider, J. Zhang, Y. Pei, J. Wang, X. Zhan, S. R. Marder,
15 M. F. Toney, F. So, G. N. M. Reddy and J. R. Reynolds, *Chem. Mater.*, 2022, **34**, 6853–6867.
- 16 36 J. Kang, S. Y. Kim, H. H. Jo and K. Zong, *ChemSusChem*, 2024, **17**, e202400216.
- 17 37 Z. Abid, L. Ali, S. Gulzar, F. Wahad, R. S. Ashraf and C. B. Nielsen, *Beilstein J. Org.*
18 *Chem.*, 2023, **19**, 1694–1712.
- 19 38 D. Gedefaw, M. Prosa, M. Bolognesi, M. Seri and M. R. Andersson, *Adv. Energy Mater.*,
20 2017, **7**, 1700575.
- 21 39 J. Yuan, J. Ouyang, V. Cimrová, M. Leclerc, A. Najari and Y. Zou, *J. Mater. Chem. C*,
22 2017, **5**, 1858–1879.
- 23 40 P.-Y. Gu, Z. Wang, G. Liu, H. Yao, Z. Wang, Y. Li, J. Zhu, S. Li and Q. Zhang, *Chem.*
24 *Mater.*, 2017, **29**, 4172–4175.
- 25 41 S. Riera-Galindo, M. Sanz-Lleó, E. Gutiérrez-Fernández, N. Ramos, M. Mas-Torrent, J.
26 Martín, L. López-Mir and M. Campoy-Quiles, *Small*, 2024, **20**, 2311735.
- 27 42 J. Barron, S. Attar, A. Ghobadi, S. Gangopadhyay, D. Sredojevic, M. Al-Hashimi and S.
28 Guha, *ACS Appl. Electron. Mater.*, 2024, **6**, 1464–1474.
- 29 43 S. Gámez-Valenzuela, S. Ma, Y. Wei, Y. Lu, C. Xu, K. Feng, S. Y. Jeong, H. Wang, H. Y.
30 Woo, A. Facchetti and X. Guo, *J. Am. Chem. Soc.*, 2025, **147**, 38851–38864.
- 31 44 H. Jung, K. Nakano and K. Tajima, *ACS Appl. Mater. Interfaces*, 2025, **17**, 66980–66987.
- 32 45 T. Mikie, K. Okamoto, Y. Iwasaki, T. Koganezawa, M. Sumiya, T. Okamoto and I. Osaka,
33 *Chem. Mater.*, 2022, **34**, 2717–2729.



- 1 46 Z. Dai, D. Zhang and H. Zhang, *Front. Chem.*, 2022, **10**, 934203.
- 2 47 J. Jeon, H. Jhon, M. Kang, H. J. Song and T. K. An, *Org. Electron.*, 2018, **56**, 1–4.
- 3 48 B. Ma, Q. Shi, X. Ma, Y. Li, H. Chen, K. Wen, R. Zhao, F. Zhang, Y. Lin, Z. Wang and
4 H. Huang, *Angew. Chem. Int. Ed.*, 2022, **61**, e202115969.
- 5 49 J. Kimpel, Y. Kim, H. Schomaker, D. R. Hinojosa, J. Asatryan, J. Martín, R. Kroon, M.
6 Sommer and C. Müller, *Sci. Adv.*, 2025, **11**, eadv8168.
- 7 50 R. Po, G. Bianchi, C. Carbonera and A. Pellegrino, *Macromolecules*, 2015, **48**, 453–461.
- 8 51 M. Mamone, T. Bura, S. Brassard, E. Soligo, K. He, Y. Li and M. Leclerc, *Mater. Chem.*
9 *Front.*, 2020, **4**, 2040–2046.
- 10 52 T. Lei, J. H. Dou, X. Y. Cao, J. Y. Wang and J. Pei, *Adv. Mater.*, 2013, **25**, 6589–6593.
- 11 53 P. C. Rodrigues, L. S. Berlim, D. Azevedo, N. C. Saavedra, P. N. Prasad, W. H. Schreiner,
12 T. D. Z. Atvars and L. Akcelrud, *J. Phys. Chem. A*, 2012, **116**, 3681–3690.
- 13 54 D. Yuan, G. Qin, L. Zhang, F. Pan, R. Qiu, S. Lei and J. Chen, *ACS Appl. Mater. Interfaces*,
14 2021, **13**, 57654–57663.
- 15 55 C. Yorur Goreci, M. Kazici, S. Bozar, H. Gokce and S. Gunes, *J. Mater. Sci.: Mater.*
16 *Electron.*, 2021, **32**, 14749–14763.
- 17 56 W. He, Q. Liu, S. Otep, H. Matsumoto, S. Manzhos, P. Sonar, A. K. K. Kyaw and T.
18 Michinobu, *Chin. J. Chem.*, 2023, **41**, 1028–1036.
- 19 57 Q. Liu, S. Kumagai, S. Manzhos, Y. Chen, I. Angunawela, M. M. Nahid, K. Feron, S. E.
20 Bottle, J. Bell, H. Ade, J. Takeya and P. Sonar, *Adv. Funct. Mater.*, 2020, **30**, 2000489.
- 21 58 M. Waldrip, O. D. Jurchescu, D. J. Gundlach and E. G. Bittle, *Adv. Funct. Mater.*, 2020,
22 **30**, 1904576.
- 23 59 K. Shibata, H. Wada, K. Ishikawa, H. Takezoe and T. Mori, *Appl. Phys. Lett.*, 2007, **90**,
24 193509.
- 25 60 D. K. Tran, A. Robitaille, I. J. Hai, C.-C. Lin, D. Kuzuhara, T. Koganezawa, Y.-C. Chiu,
26 M. Leclerc and S. A. Jenekhe, *Chem. Mater.*, 2022, **34**, 9644–9655.
- 27 61 N. E. Persson, P. H. Chu, M. McBride, M. Grover and E. Reichmanis, *Acc. Chem. Res.*,
28 2017, **50**, 932–942.
- 29 62 J. Rivnay, S. C. B. Mannsfeld, C. E. Miller, A. Salleo and M. F. Toney, *Chem. Rev.*, 2012,
30 **112**, 5488–5519.
- 31 63 J. H. Kim, C. E. Song, W. S. Shin, B. Kim, I. N. Kang and D. H. Hwang, *J. Polym. Sci.*
32 *Part A: Polym. Chem.*, 2015, **53**, 1904–1914.



- 1 64 R. Noriega, J. Rivnay, K. Vandewal, F. P. V. Koch, N. Stingelin, P. Smith, M. F. Toney
2 and A. Salleo, *Nat. Mater.*, 2013, **12**, 1038–1044.
- 3 65 C. G. Tang, K. Hou and W. L. Leong, *Chem. Mater.*, 2024, **36**, 28–53.
- 4 66 J. Choi, M. J. Kim, J. Y. Kim, E. K. Lee, C. Lee, Y. Park, J. Kang, J. Il Park, B. J. Cho and
5 S. G. Im, *Small Methods*, 2023, **7**, 2300628.
- 6 67 S. Guchait, L. Herrmann, K. Kadri, N. Leclerc, F. Tran Van and M. Brinkmann, *ACS Appl.*
7 *Polym. Mater.*, 2023, **5**, 5676–5686.
- 8 68 Y. Kim, H. Park, J. S. Park, J. W. Lee, F. S. Kim and B. J. Kim, *J. Mater. Chem. A*, 2022,
9 **10**, 2672–2696.
- 10 69 Y. Otake and T. Amaya, *Synth. Met.*, 2025, **314**, 117922.



Data Availability Statement

Cost-efficient quinoxaline-based semiconducting polymers: systematic structure–property–morphology correlation toward reliable organic field-effect transistors

Yuta Otake, Atsushi Isobe, Ting-Yu Wang, Chu-Chen Chueh, Masayuki Wakioka, and Tsuyoshi Michinobu*

Data availability:

The data that support the findings of this study are available from the corresponding author upon reasonable request.

